www.springer.com/41230
https://doi.org/10.1007/s41230-025-4178-y
Research & Development
Vol. 22 No. 5 September 2025
CHINA FOUNDRY

Vat photopolymerization of silica-based ceramic cores using high solid loading slurry with performance optimization

Yong-kang Yang[1], Bo-ran Wang[2], Zi-qi Jia[1], *Shu-xin Niu[3], Xin Li[3], Ya-jie Guo[1], and **Xi-qing Xu[1]

1. School of Materials Science and Engineering, Chang'an University, Xi'an 710061, China

2. School of Materials Science and Engineering, Key Lab of Advanced Ceramics and Machining Technology of Ministry of Education, Tianjin University, Tianjin 300072, China

3. Science and Technology on Advanced High Temperature Structural Materials Laboratory, Beijing Institute of Aeronautical Materials, Beijing 100095, China

Abstract: Vat photopolymerization (VPP) 3D printing is an optimized technology for complex-shaped ceramic cores, in which the solid loading of ceramic slurries greatly influences the microstructure and property of the final ceramic parts. However, the high solid loading of slurries is highly limited by the high viscosity. In this study, silica-based ceramic core slurries with solid loading up to 68vol.% were achieved by the composition design to optimize the performance, considering the curing, rheological, and double bond conversion rate. The slurries demonstrate superior curing and rheological performance with mass ratio of monomers being 3:2 and mass fraction of BYK111 being 4wt.%. Afterwards, the impact of solid loading on the morphology and mechanical properties was investigated. As the solid loading increases, the microstructure becomes gradually dense, leading to an improved flexural strength of 19.5 MPa. Additionally, the sintering shrinkage becomes more uniform, satisfying the casting requirements effectively. This work serves as a guide for the preparation of ceramic slurries with a high solid loading.

Keywords: ceramic core; additive manufacturing; mechanical performance; solid loading; viscosity; vat photopolymerization

CLC numbers: TG221 **Document code:** A **Article ID:** 1672-6421(2025)05-555-10

1 Introduction

Ceramic cores, serve as crucial components in aero-engine turbine blades, enable the formation of complex internal structures that facilitate air-cooling for the blades [1-5]. The advancement of the aerospace industry has called for higher and higher temperature of the engine inlet to enhance the thrust-to-weight ratio [6, 7]. Consequently, the requirements for the internal cooling structure must be increasingly strict. As a result, the design of ceramic cores has evolved towards being multi-layered and complex [8]. Currently, hot injection molding is the traditional process used for fabricating ceramic cores; nevertheless, it is mostly dependent on molds and faces challenges in producing ceramic cores with intricate structures [9,10]. The high cost of molds and the long research and development cycle consistently hinder the progress of ceramic core development [11]. Hence, the fabrication of ceramic cores featuring complex, three-dimensional structures necessitates the establishment of a novel preparation process tailored to their geometrical intricacies.

The ceramic cores can now be manufactured via an innovative approach due to the rapid development of ceramic additive manufacturing, which can break through the restrictions of molds for ceramic molding,

***Shu-xin Niu**

Male, born in 1987, Senior Engineer. His research interests mainly focus on single crystal blade casting technology and ceramic core technology.

E-mail: shuxinniu123@163.com

****Xi-qing Xu**

Male, born in 1990, Ph. D., Associate Professor. His research interests mainly focus on the preparation technology of new ceramic materials, additive manufacturing technology and its application in the aerospace and weapon industry.

E-mail: xiqingxu@chd.edu.cn

Received: 2024-08-23; Revised: 2024-11-11; Accepted: 2024-12-05

and significantly shorten the research and development cycle and reduce production costs [12-15]. Among various additive manufacturing technologies, vat photopolymerization (VPP) 3D printing is relatively mature with the benefits of high accuracy and excellent surface quality [16, 17]. Li et al. [18] employed an Ar atmosphere to regulate the oxidation of Al powders and utilized liquid-phase sintering to enhance the performance of alumina-based cores, which led to low linear shrinkage of 0.3%. Niu et al. [19] doped mullite fibers into a silica-based ceramic core to enhance the dimensional accuracy, and the high-temperature deflection was decreased to 1.79 mm. Li et al. [20] revealed the anisotropy mechanism of VPP-3D printing through finite element simulation and optimized the physical properties of the ceramic cores via designed sintering regime. The above research demonstrates the viability of producing ceramic cores through VPP-3D printing technology.

The high solid loading of ceramic slurries for VPP-3D printing, not only provides reliable strength for sintered parts, but also reduces shrinkage, which is particularly important for ceramic cores [21-23]. To attain a ceramic slurry with high solid loading and excellent rheological properties, Zhang et al. [24] obtained a 60vol.% ceramic slurry with a low viscosity of 15.4 Pa·s at 200 s^{-1} through a systematic study of dispersants. Fan et al. [25] used a dual dispersant to enhance the uniform dispersion of ceramic particles in the photosensitive resin and obtained a solid loading of 70vol.%; however, the porosity of 20.7% hindered the subsequent leaching. Jin et al. [26] prepared a ceramic slurry with 60vol.% solid loading by controlling the resin composition, which showed excellent curing properties. Nevertheless, the shrinkage after sintering was around 8%, which limited the dimensional accuracy of the ceramic core. Therefore, the choice of solid loading for VPP-3D printing ceramic cores remains to be optimized.

In general, ceramic cores prepared using VPP-3D printing contain more than 40vol.% of photosensitive resin, which gives rise to deformation during debinding and sintering and high sintering shrinkage [27,28]. In order to obtain silica-based ceramic cores with excellent performance, ceramic slurries with high solid loading and appropriate viscosity are important prerequisites. Therefore, it is necessary to comprehensively analyze the various components in order to get high-quality ceramic slurry [29].

In this study, a comprehensive investigation was conducted on the impact of monomer ratio and dispersant on the curing and rheological properties of slurries, and the optimized photosensitive resin composition was obtained. The solid loading was up to 68vol.% by adjusting the proportion of resin to ceramic powder, and the effects on the curing performance, microstructure evolution, and mechanical properties of ceramic cores were studied. This work serves as a guide for the formulation of ceramic core slurries with a high solid loading.

2 Experimental procedures

2.1 Raw materials

The matrix material selected was fused silica (D_{50}=4.89 μm, >99.95%), and alumina (D_{50}=24.8 μm, >99.99%, Lianyungang Xinhai Quartz Products Co., Ltd.) and $ZrSiO_4$ (D_{50}=23.6 μm, >99.99%, Aladdin Biochemical Technology Co., Ltd.) were employed as mineralizers to improve the physical characteristics of the ceramic cores. The SEM images of the raw materials are depicted in Figs. 1(a–c). The primary constituents of the photosensitive resin consisted of 1,6 hexanediol diacrylate (HDDA) and trimethylolpropane triacrylate (TMPTA), which were procured from Shanghai Aladdin Co., Ltd. Dispersants BYK180, BYK9076, BYK111 (BYK Limited, Germany), and KOS110 (Guangzhou Kang'oushuang Trade Co., Ltd., China) were selected to assess their effects on the rheological characteristics of ceramic slurries. Diphenyl (2,4,6-trimethylbenzoyl) phosphine oxide (TPO, Shanghai Yinchang Co., Ltd., China) was chosen as a photoinitiator to produce a cross-linking curing reaction under ultraviolet light irradiation.

2.2 Slurry and ceramic core sample preparation

Fused silica, alumina, and $ZrSiO_4$ were mixed at a mass ratio of 85:10:5. Subsequently, a mixture of TPO and dispersant was combined with a mixed monomer consisting of HDDA and TMPTA to form a premixed liquid. The detailed compositions of premixed liquid are listed in Tables 1 and 2. Thereafter, the ceramic powder and photosensitive resin were placed into a planetary ball mill and mixed at 600 rpm for 4 h. The ceramic slurries were prepared by adjusting the proportion of ceramic powder and photosensitive resin to achieve solid loading of 56vol.%, 60vol.%, 64vol.%, and 68vol.%.

The SolidWorks software was utilized to construct test rods with 60 mm×10 mm×4 mm, according to the HB5353 standard. The prepared ceramic slurry was placed into the ceramic 3D printer (Autocera-L, Beijing Ten Dimension Technology Co., Ltd., China). The wavelength of ultraviolet

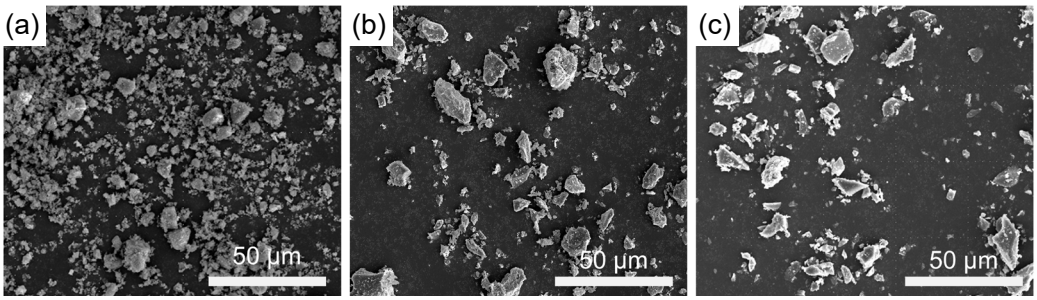

Fig. 1: SEM images of raw materials: (a) fused silica; (b) Al_2O_3; (c) $ZrSiO_4$

Table 1: Composition of the premixed liquid

Label	HDDA:TMPTA (wt.%)	Dispersant concentration (wt.%)	Solid loading (vol.%)
1	4:1	2	56
2	3:2	2	56
3	2:3	2	56
4	1:4	2	56

Table 2: Detailed information of ceramic core slurries based on varying dispersant types and dispersant concentrations

Label	Types	Dispersant concentration (wt.%)	Solid loading (vol.%)
1	BYK111	2	56
2	BYK180	2	56
3	BYK9076	2	56
4	KOS110	2	56
5	BYK111	1/2/3/4/5	56
6	BYK111	4	56/60/64/68

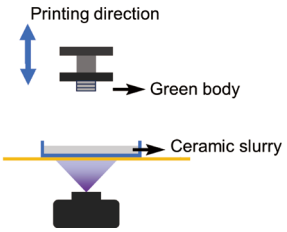

Fig. 2: Schematic of VPP-3D printing

(UV) light employed was 405 nm, the thickness of the slice layer was 100 μm, the duration of exposure was set to 3 s, and the power was in the range of 6–10 mW·cm^{-2}. The schematic diagram of the VPP-3D printing process is shown in Fig. 2

2.3 Debinding and sintering process

To ascertain the temperature at which the photosensitive resin decomposes in the air, the green body was analyzed by TG-DTG (TA Netzsch, Germany) with a heating rate of 10 °C·min^{-1}. Figures 3(a–b) illustrate the complicated procedure of debinding and sintering. The green body was heated to 200 °C at 1 °C·min^{-1} in a muffle furnace and held for 1 h. Subsequently, it was heated to 395 °C, 495 °C, and 581 °C at a rate of 0.2 °C·min^{-1}, with each temperature maintained for 2 h. Afterwards, the temperature was elevated to 1,200 °C at a rate of 2 °C·min^{-1}, and the sample was maintained for 6 h, and cooled to the ambient temperature in the furnace, resulting in the formation of a silica-based ceramic cores.

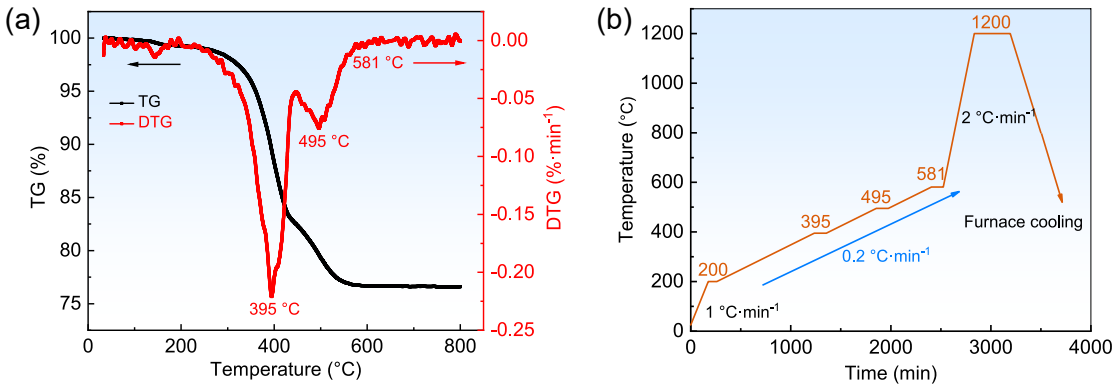

Fig. 3: TG-DTG curves (a) and sintering regime (b) of ceramic green body

2.4 Characterization

The rheological characteristics of the ceramic slurries were evaluated using a rheometer (MARS40, FEI, USA) under controlled ambient conditions, with shear rates ranging from 0.1 to 200 s^{-1}. Using Fourier infrared spectroscopy (Nicolet iS10, FEI, USA), the surface groups of the slurries and powders were identified. Analysis of the microstructure of ceramic cores by SEM (Nova450, FEI, USA) was performed to understand the process of evolution. The phase constitution of the sintered ceramic core was investigated via X-ray diffraction (D8 Advance, Bruker, Germany) using a Cu target, with a range spanning from 10° to 90°. An optical microscope (SZX10, OLYPUS, Japan) was employed to measure the overgrowth width of curing samples. The porosity and bulk density were determined by the Archimedes' method, and the flexural strength was measured using an electronic universal testing machine (WDW-10, Changchun Kexin Co., Ltd., China) with a span of 30 mm. Using a vernier calliper, the dimensions of the sample before and after the sintering stage were measured to calculate the shrinkage.

3 Results and discussion

3.1 Impact of component design on preparation of ceramic slurry

3.1.1 Impact of different monomer ratios

Figure 4(a) depicts the rheological properties of silica-based ceramic slurries with solid loading of 56vol.% at different

monomer ratios. The number of functional groups generally has a positive correlation with the slurry viscosity, as the higher functional groups lead to stronger intermolecular interactions, resulting in increased viscosity [26]. HDDA, as a bifunctional monomer, can reduce slurry viscosity and curing shrinkage, while TMPTA, as a trifunctional monomer formed a network structure, which can be crosslinked and polymerized during the photopolymerization to achieve a green body with high strength.

To verify the stability of slurries with different monomer ratios, sedimentation experiments were carried out under the actual application environment (room temperature of 25 °C and humidity of 45%), with an experimental period of 14 days. Figure 4(b) depicts a schematic of the sedimentation test of a ceramic slurry, where H_0 denotes the initial volume of the slurry, and H_1 corresponds to the volume of clarified liquid obtained after the settling process. The effect of different monomer proportions on sedimentation is shown in Figs. 4(c, d). It can be seen with the increase of HDDA content, the sedimentation ratio of slurry increases from 1.75% to 4.73%, and the stability gradually decreases. The sedimentation of the ceramic slurry is mainly significantly affected by the Brownian motion, and the settling velocity of the slurry can be evaluated using the Stokes settlement velocity equation [30]:

$$v_0 = \frac{H_1}{T} = \frac{(\rho_p - \rho_r)g}{18\mu} D^2 \quad (1)$$

where v_0 represents settling velocity, D represents the diameter of a spherical particle, ρ_p and ρ_r are the particle density and slurry density, respectively, g represents the gravitational acceleration, and μ represents the viscosity of the slurry. The results show that the settling rate of the slurry is mainly determined by its viscosity and particle size, with all other conditions remaining constant. As the proportion of HDDA increases, the number of functional groups in the slurry decreases, so the viscosity gradually decreases, which destroys the stability of the slurry. Therefore, it is crucial to maintain an appropriate viscosity to ensure the stability of high-performance ceramic slurries.

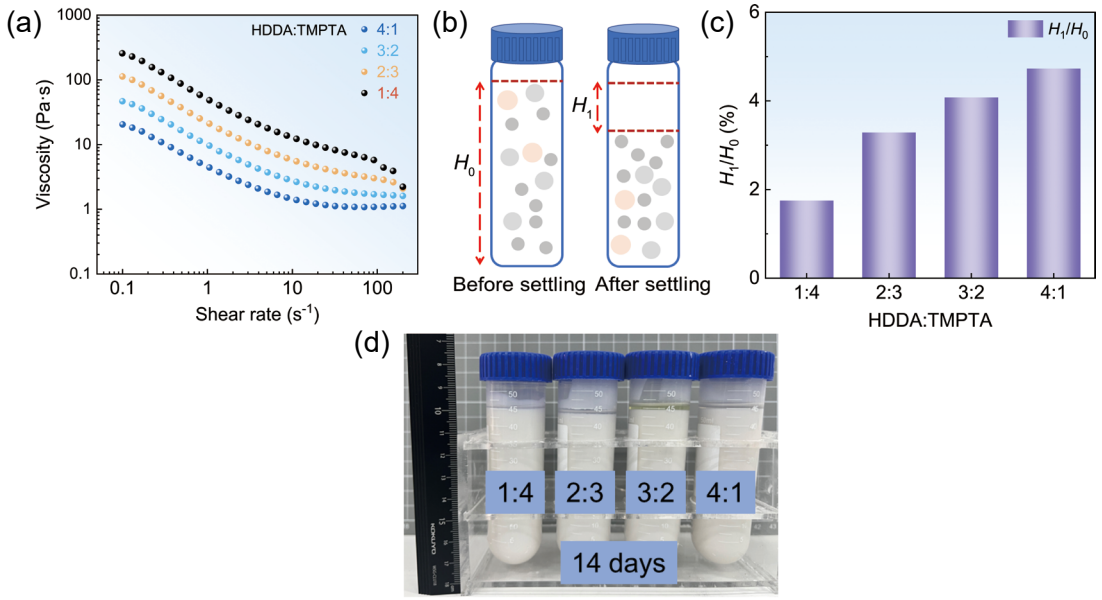

Fig. 4: Effect of varying monomer ratios on the viscosity of ceramic slurries (a), schematic diagram of sedimentation test of ceramic slurries (b), a relationship of H_1/H_0 volume fraction after 14 days settling (c), and sedimentation results of slurry at different monomer ratios (d)

In the VPP-3D printing process, the selection of printing parameters is crucial for the curing depth and curing accuracy of ceramic slurries. In order to obtain high printing quality, the curing properties of different slurries were investigated. Figure 5(a) indicates the statistics of printing parameters on the curing depth of ceramic slurries with varying monomer ratios. The curing depth increases with the increase of exposure power, which can provide better interlayer bonding of green body and ensure the dimensional accuracy of ceramic cores. The curing behavior of the ceramic slurry is mainly affected by the number of functional groups in the photosensitive resin, and the increase in the content of functional groups results in a faster curing speed, which allows the rapid formation of a crosslinked mesh structure and a gradual increase in the curing depth under UV light irradiation [26].

In order to further analyze the effect of the monomer ratio on the vat photopolymerization reaction, it was characterized by the Beer-Lambert law [31]:

$$C_d = D_p \ln\left(\frac{E_0}{E_c}\right) = D_p \ln E_0 - D_p \ln E_c \quad (2)$$

where C_d represents the curing depth (μm), the physical quantity D_p is associated with the attenuation coefficient, whereas the critical exposure energy E_c (mJ·cm^{-2}) was measured, which is the least amount of exposure energy needed to start the polymerization of the resin. E_0 indicates the actual exposure energy (mJ·cm^{-2}). Typically, a lower E_c is considered favorable for the VPP-3D printing process. The fitting results are shown in Fig. 5(b), with the increase of TMPTA content, the slope D_p and the depth of curing show

an increasing trend, indicating the positive effect of the number of functional groups on the photopolymerisation reaction.

The mechanism of E_c change was further analyzed by evaluating the conversion of C=C before and after curing of the ceramic slurries by FT-IR, as shown in Fig. 5(c). In the FT-IR spectra, the C=O stretching vibration peak locates at 1,722 cm^{-1} remains stable before and after curing, which can be used as an internal standard for evaluating the photopolymerization reaction. By analyzing the intensity evolution of the C=C peaks at 1,410 cm^{-1} and 1,620 cm^{-1}, the double bond conversion rate of the ceramic slurries was calculated with the following equation [32]:

$$\alpha(t)=\frac{\left[\frac{\mathrm{Area}_{1620}+\mathrm{Area}_{1410}}{\mathrm{Area}_{1722}}\right]_0-\left[\frac{\mathrm{Area}_{1620}+\mathrm{Area}_{1410}}{\mathrm{Area}_{1722}}\right]_t}{\left[\frac{\mathrm{Area}_{1620}+\mathrm{Area}_{1410}}{\mathrm{Area}_{1722}}\right]_0}\times 100\% \quad (3)$$

The fitting results of E_c and the C=C conversion rate are shown in Fig. 5(d). With the increase of TMPTA content, the E_c of ceramic slurries shows a trend of decreasing firstly and then increasing, while the trend of C=C conversion rate is opposite. This is mainly attributed to the synergistic effect of the number of monomer functional groups and viscosity in ceramic slurries. Initially, the number of functional groups increases with increasing TMPTA content, which accelerates the formation of a reticulated polymer from the photosensitive resin, and the conversion rate thus rises. Subsequently, an excess of TMPTA hinders the mobility of free radicals in the slurry and the conversion of C=C double bonds is limited, which is confirmed by the change in slurry viscosity, as shown in Fig. 4(a) [33, 34].

Based on the discussion above, the selection of a monomer ratio requires a balance between the viscosity and the curing characteristics. Eventually, the mass ratio of HDDA:TMPTA=3:2 was selected for follow-up experiment.

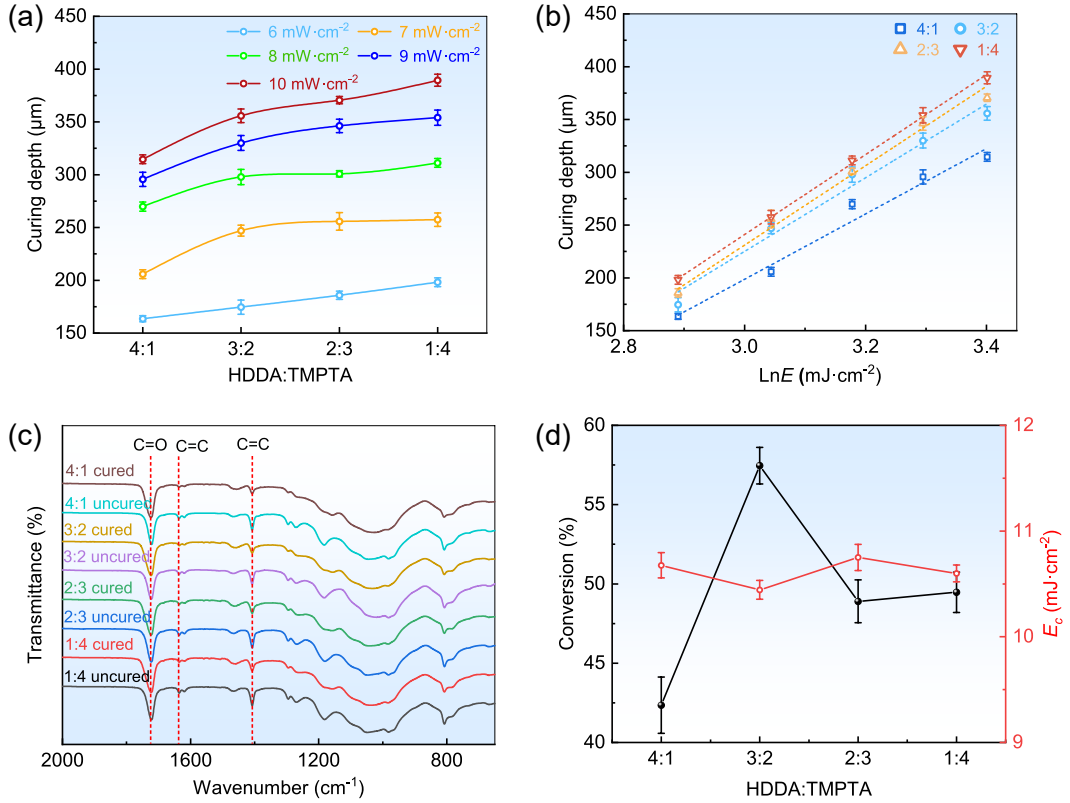

Fig. 5: Effect of varying monomer ratios on photopolymerization reaction: (a) curing depth; (b) Beer-Lambert law fitting results; (c) full FT-IR spectra; (d) conversion rate of C=C and value of E_c

3.1.2 Mechanism analysis of dispersant on ceramic slurry

To probe the most suitable slurry system, BYK111, BYK180, BYK9076, and KOS110 were selected as dispersants, and rheological tests were carried out, respectively. The solid loading was 56vol.%, and the initial dispersant concentration was 2wt.%. Figure 6(a) depicts the rheological property of ceramic slurries with different dispersant types, in which BYK111 shows the best dispersion performance and significantly decreased viscosity. According to the manufacturer's documentation and references [35-37], KOS110, BYK180, and BYK9076 are polyacrylates, alkylhydroxy ammonium salts, and alkylammonium salts, respectively, whereas BYK111 is structurally composed of ester and alkyl hydrocarbon groups. Considering the interfacial compatibility, the hydrophobic group of BYK111 can show good compatibility with acrylate-based photosensitive resins with higher interfacial affinity [35]. The viscosity of BYK111, measured at a shear rate of 10 s^{-1}, is determined to be 2.65 Pa·s, enabling its suitability for vat photopolymerization applications. The material exhibits non-Newtonian shear thinning behavior, as

evidenced by the reduction in viscosity under shear stress exerted by the scraper during printing. This property facilitates the effective spreading of the ceramic slurry and enhances the overall printing process. Additionally, the reduced viscosity effectively prevents printing flaws from arising and encourage substance diffusion during the photopolymerization procedure, which is advantageous for manufacturing high-precision ceramic cores.

Figure 6(b) demonstrates that the concentration of BYK111 dispersant has a notable impact on the viscosity of the ceramic slurries. The viscosity exhibits an initial fall followed by an increase as the concentration of dispersant increases. When the dispersant concentration is 4wt.%, the slurry viscosity achieves its minimum value of 1.22 Pa·s at a shear rate of 200 s^{-1}. In addition, the viscosity rises to 1.43 Pa·s when the dispersant concentration reaches 5wt.%. There are not enough ceramic particles to cover the area when the dispersant concentration is inadequate. The extra particles clash with one another through Brownian motion, causing agglomeration and adhesion. Nevertheless, too many dispersant molecules will be in the interparticle framework, which will cause flocculation and raise the viscosity of the slurry. Therefore, in this experiment, the optimal concent of BYK111 dispersant is 4wt.%.

Thus, BYK111 with a content of 4wt.% was employed as a dispersant in this experiment, whose chemical composition was a phosphate ester polymer containing acidic groups. FT-IR analysis of ceramic powder and ceramic slurry containing 4wt.% of BYK111 was carried out to confirm the mechanism of the dispersant. As indicated in Fig. 6(c), the ceramic powder shows main absorption peaks at 1,027 cm^{-1} (Si-O-Si) and 795 cm^{-1} (Si-O-Si), respectively. Meantime, the hydrophilic ceramic particles are identified by the hydroxyl groups at 3,389 cm^{-1} and 1,643 cm^{-1}, which ensures the dispersant to alter the particle surface [35]. For the slurries, the new absorption peaks mean a change in the particle surface groups. The asymmetrical stretching vibration of -CH_2 is responsible for the peaks at 2,939 cm^{-1} and 2,864 cm^{-1}, and the primary peaks of unsaturated double bonds in HDDA and TMPTA are 1,635 cm^{-1} (C=C) and 807 cm^{-1} (C=C), respectively [36]. At the same time, the C=O is located at 1,722 cm^{-1}. Since the mixing methods were mechanical stirring and ball milling, the Si-O-Si is slightly offset compared to ceramic powder (1,018 cm^{-1}).

The results of FT-IR spectroscopy demonstrate that the ceramic powder is uniformly coated with BYK111 dispersant. The dispersant in the slurry mainly acts on the surface group of ceramic particles, which effectively solves the problem of poor wettability of ceramic particles in photosensitive resins. In this experiment, ester groups and alkanes constitute the hydrophobic group of BYK111 when interfacial compatibility is considered, which exhibits good compatibility with acrylic-based resins [30]. The dispersant is eventually adsorbed onto the surface of ceramic particle through a combination of van der Waals forces, covalent bonds, and hydrogen bonds. It then interacts with the resin to reach equilibrium, enhancing the stability and rheological of the slurry [37].

3.1.3 Impact of solid loading on ceramic slurries

The slurry viscosity with varying solid loading is plotted versus the shear rates in Fig. 7(a). A noticeable rise in viscosity is observed as the solid loading increases. This is because the ceramic particles stack at a higher density, raising the resistance to friction between the particles.

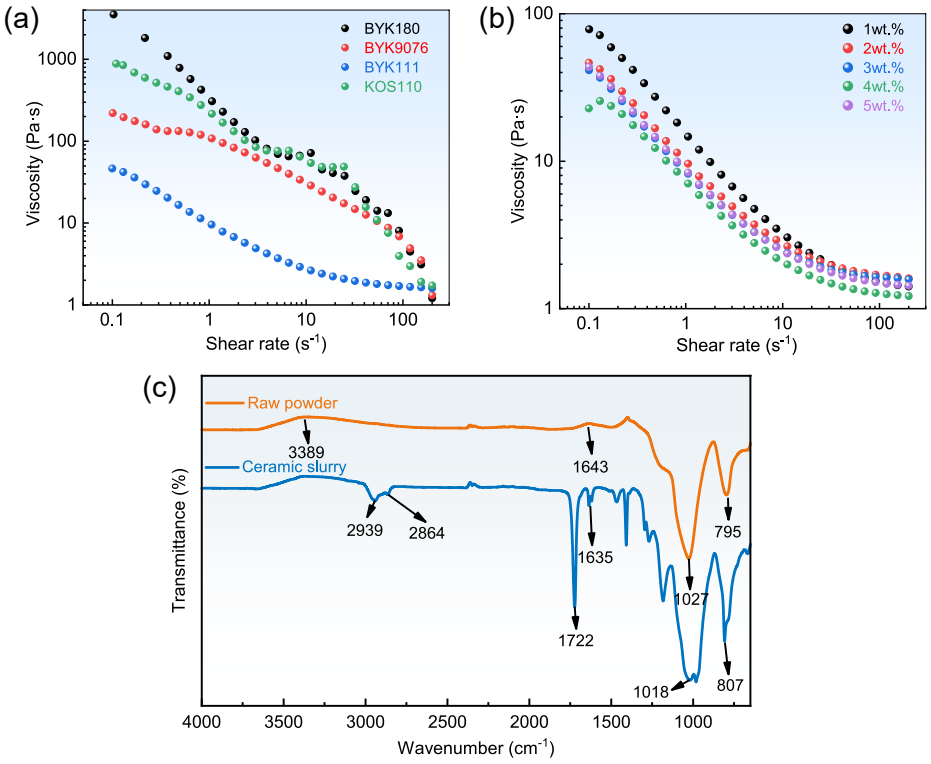

Fig. 6: Viscosity of ceramic slurries with different types of dispersants (a), different concentrations of BYK111 dispersant (b), and FT-IR analysis of raw powders and ceramic slurries (c)

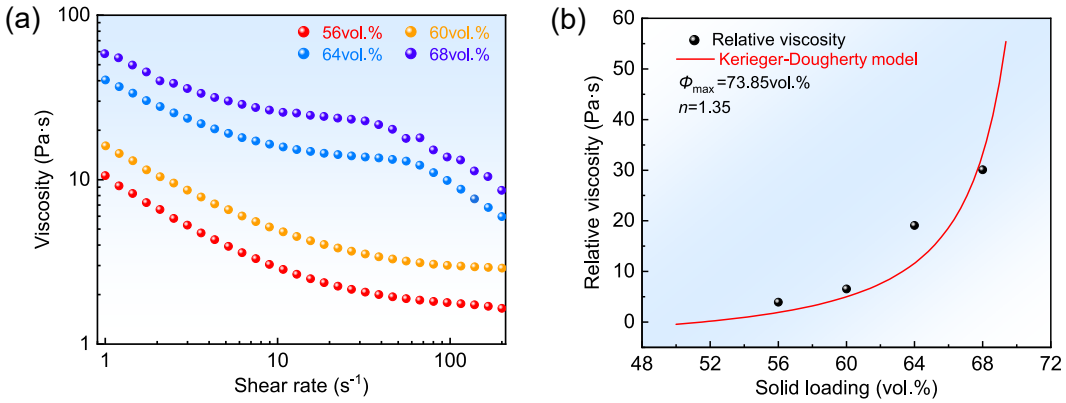

Fig. 7: Viscosity of ceramic slurries with varying solid loadings (a) and fitting of relative viscosity versus solid loading at a shear rate of 5 s^{-1} (b)

Based on the Krieger-Dougherty viscosity model, Fig. 7(b) illustrates the fitting of the slurry viscosity at a shear rate of 5 s^{-1}, as represented by [38]:

$$\eta = \left(1 - \frac{\Phi}{\Phi_{max}}\right)^{-n} \quad (3)$$

where Φ and Φ_{max} represent the volume fraction and maximum volume fraction of ceramic particles in the slurry, respectively, η denotes the relative viscosity, and the fitting parameter is represented by n. The fitting results demonstrate that the viscosity at a solid loading is in line with this model. The irregularity of particle shapes is responsible for the deviations from the Krieger-Dougherty model, with the effective volumetric solid loading differing more from the theoretical values as the degree of shape irregularity increases [39]. By analyzing rheological propertyies, it is determined that a ceramic slurry with a solid loading of 68vol.% is appropriate for VPP-3D printing.

The overgrowth width of the ceramic slurry was measured via an optical microscope to examine the impact of solid loading on exposure performance, as depicted in Figs. 8(a–d). The overgrowth width becomes higher with increasing solid loading and the cured sample profile gradually transforms from a smooth surface to a jagged one, indicating that the printing accuracy is deteriorated, attributed to the scattering effect of ceramic particles on UV light. During the ceramic light-curing process, the path of propagation of the UV light changes due to the interaction of the UV light with the photosensitive resin and the ceramic particles, which reduces the penetration of the light and results in a lower curing depth.

The interaction mechanism between UV light with ceramic particles is shown in Fig. 9(a). When the solid loading is gradually increased, the particles are easily agglomerated and the flowability is deteriorated, resulting in a higher viscosity. Furthermore, the large number of ceramic particles would enhance the absorption and scattering of UV radiation, resulting in a sharp increase in the overgrowth width, which has a direct impact on the forming precision of the VPP-3D printing ceramic cores, as depicted in Fig. 9(b). Figure 10 demonstrates the high structural complexity of the printed sample, indicating that the slurry with a solid loading of 68vol.% is capable of meeting the printing demand.

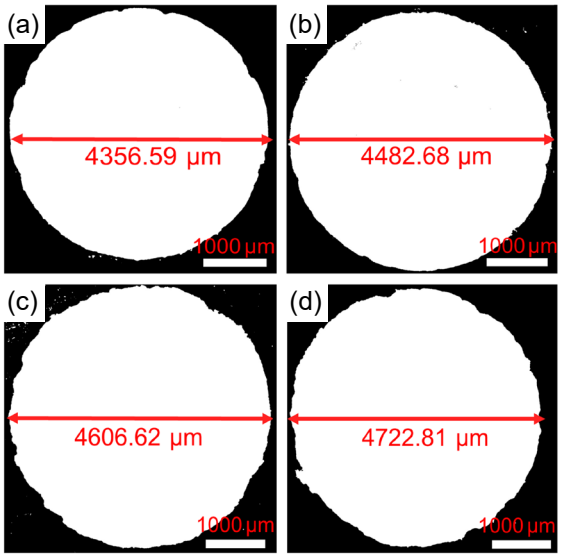

Fig. 8: Effect of varying solid loading on overgrowth width: (a) 56vol.%; (b) 60vol.%; (c) 64vol.%; (d) 68vol.%

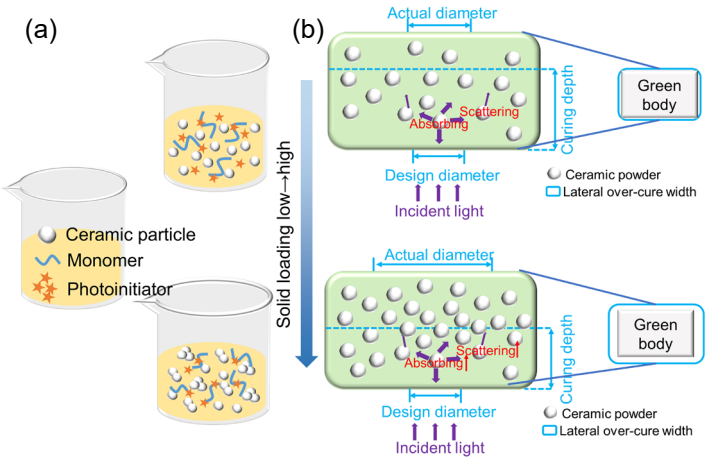

Fig. 9: Schematic of varying solid loading slurries (a) and schematic of mechanism of light scattering by high solid loading (b)

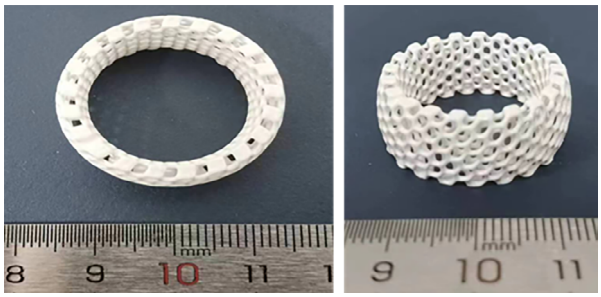

Fig. 10: Samples with complex structures

3.2 Performance analysis of VPP-3D printing ceramic cores

3.2.1 Microstructure evolution and element distribution

Figures 11 depict the cross-section and surface microstructure after sintering with different solid loading, where Figs. 11(a–d) are the cross-section and Figs. 11(a1–d1) are the surface (red circles with arrows indicate pores and yellow arrows indicate cracks). With the low solid loading, there are clearly visible cracks and porosity within the cores. As the solid loading

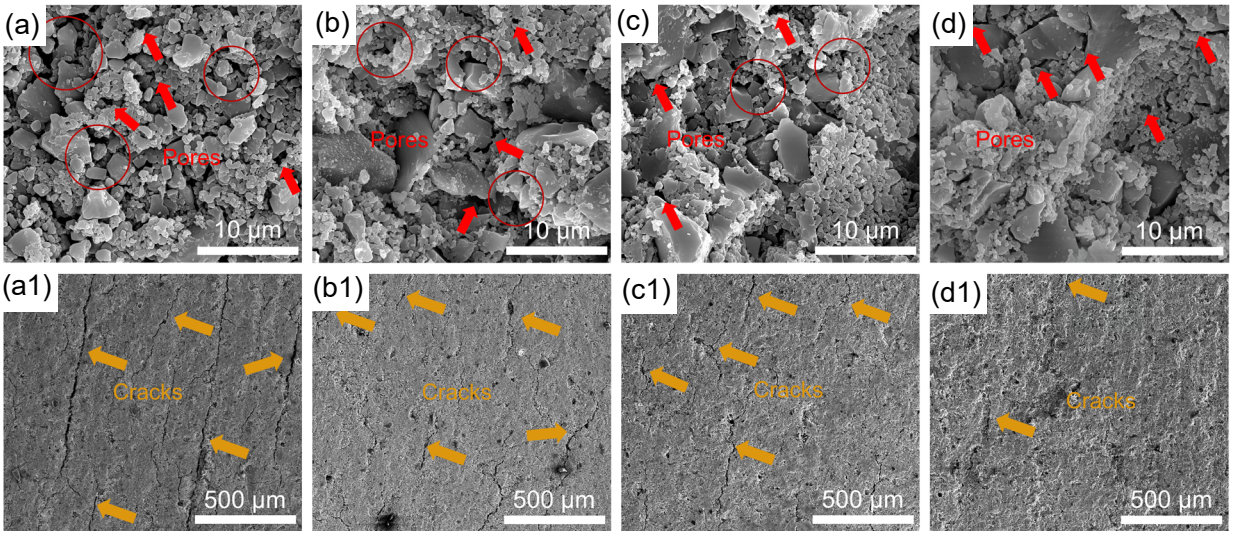

Fig. 11: Impact of varying solid loading on microstructure evolution in cross-section (a–d) and surface (a1–d1): (a–a1) 56vol.%; (b–b1) 60vol.%; (c–c1) 64vol.%; (d–d1) 68vol.%

increases, the internal microstructure becomes denser, leading to a significant reduction in porosity and effectively preventing the formation of large-scale cracks. The cracking of ceramic cores with low solid loading is attributed to the violent breakdown of photosensitive resin during the debinding stages. Additionally, the shrinkage stress generated by the binding of the ceramic particles under the sintering driving force is also a factor causing cracks. Overall, augmenting the amount of ceramic powder enhances the bulk density within the cores, hence enhancing its mechanical properties.

Figures 12(a–b) display the distribution of elements and the EDX spectra of the cross-section of the 68vol.% ceramic core. Regarding the distribution of individual elements [Fig. 12(a)], the Si, O, and Zr elements are evenly distributed over the entire region, which is attributed to diffusion mass transfer. Additionally, the presence of Al_2O_3 particles is clearly observed, which effectively enhances the physical properties of the core. Finally, elemental separation or abnormal composition is not detected inside the matrix according to the EDX spectra.

3.2.2 Physical properties

The impact of solid loading on the bulk density and three-dimensional shrinkage of ceramic cores were investigated, as shown in Fig. 13(a). Among different directions, the *Z*-axis (printing direction) exhibits a higher shrinkage, which is attributed to the layer-by-layer process of VPP-3D printing [40].

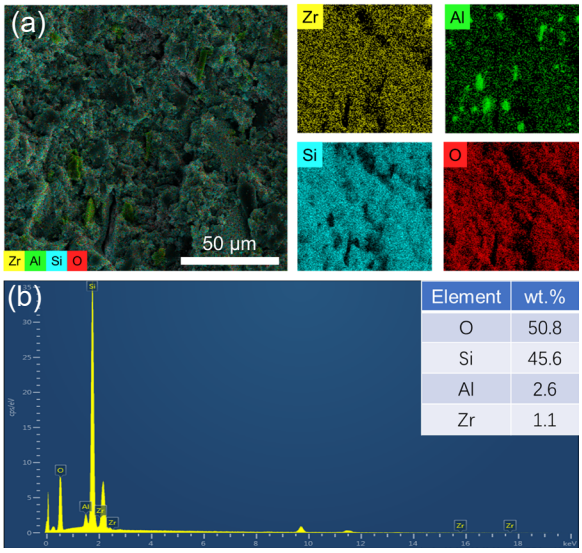

Fig. 12: Elemental distribution (a) and EDX spectra (b) of 68vol.% ceramic cores

Through raising the solid loading to 68vol.%, the shrinkage along the *Z*-axis decreases from 5.72% to 3.19%, which is close to the shrinkage in other directions, demonstrating a substantial reduction in the anisotropy of sintering shrinkage. Simultaneously, the bulk density rises to 1.75 $g \cdot cm^{-3}$, suggesting that a higher solid loading enhances more effective densification in the core, which leads to a reduction in shrinkage and an increase in bulk density.

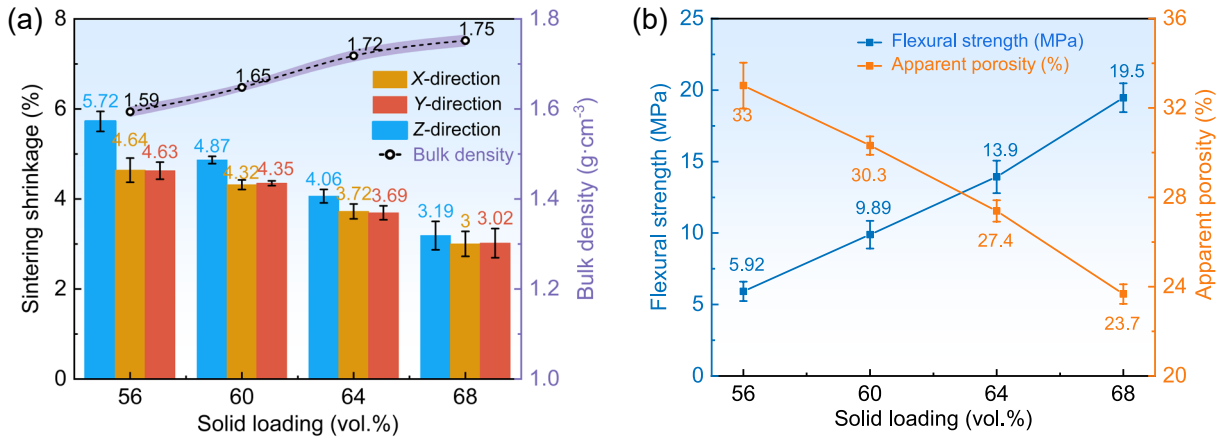

Fig. 13: Impact of varying solid loading on physical properties: (a) sintering shrinkage and bulk density; (b) flexural strength and apparent porosity

Figure 13(b) illustrates the impact of solid loading on the flexural strength and apparent porosity. The flexural strength shows a substantial enhancement, ascending from 5.92 MPa to 19.5 MPa, in correlation with increasing solid loading. Simultaneously, the apparent porosity exhibits a notable decrease, from 33% to 23.7%. The core with low solid loading contains a high proportion of photosensitive resin, which undergoes violent decomposition in the debinding and sintering process. This results in a large number of pores inside the core and an increased distance between ceramic particles. Consequently, it becomes challenging for the particles to combine with each other during sintering, leading to lower flexural strength and higher apparent porosity. An augmentation in bulk density results in a more compact microstructure, hence enhancing the physical characteristics of the ceramic core.

4 Conclusion

In this work, through the composition design of ceramic slurry to optimize the performance, including curing parameters, rheological properties, and double bond conversion rate, a slurry contains a high solid loading of 68vol.% for VPP-3D printing of silica-based ceramic core was successfully prepared. The results indicate that the slurry attains a balance between viscosity and curing performance at mass ratio of HDDA:TMPTA being 3:2. In addition, the BYK111 dispersant demonstrates to be the most appropriate for the system, with an optimal addition of 4wt.% in order to prevent coagulation. Afterwards, the impact of solid loading was thoroughly evaluated, and higher solid loading is found to enhance the densification of the microstructure, which leads to an improved flexural strength of 19.5 MPa, a low linear shrinkage of 3.19%, and a tendency towards isotropy. Although the increase in overgrowth width reduces the dimensional accuracy, this effect is minimized by coordinating the printing parameters. Overall, the prepared ceramic cores exhibit a comprehensive performance that satisfies the investment casting. This work serves as a guide for the formulation of ceramic core slurries with high solid loading.

Acknowledgments

This work was financially supported by the National Natural Science Foundation of China (No. 52102062), the Xi'an Science and Technology Plan Project (No. 23LLRH0004), and the Key Research and Development Project of Shaanxi Province of China (2024GX-YBXM-352).

Conflict of interest

The authors declare that they have no known competing financial interests or personal relationships that could have appeared to influence the work reported in this paper.

References

[1] Kanyo J E, Schafföner S, Uwanyuze R S, et al. An overview of ceramic molds for investment casting of nickel superalloys. J. Eur. Ceram. Soc., 2020, 40(15): 4955–4973.
[2] Li X, Liu Z P, Niu S X, et al. Controlled anisotropy in 3D printing of silica-based ceramic cores through oxidization reaction of aluminum powders. Ceram. Int., 2023, 49(15): 24861–24867.
[3] Xu X Q, Niu S X, Wang X G, et al. Fabrication and casting simulation of composite ceramic cores with silica nanopowders. Ceram. Int., 2019, 45(15): 19283–19288.
[4] Li X, Su H J, Dong D, et al. Enhanced comprehensive properties of stereolithography 3D printed alumina ceramic cores with high porosities by a powder gradation design. J. Mater. Sci. Technol., 2022, 131: 264–275.
[5] Liu X L, Guo X L, Shui G Y, et al. Properties of alumina-based ceramic cores. China Foundry, 2021, 18(6): 593–598.
[6] An X L, Mu Y H, Liang J J, et al. Stereolithography 3D printing of ceramic cores for hollow aeroengine turbine blades. J. Mater. Sci. Technol., 2022, 127: 177–182.
[7] An X L, Mu Y H, Chen J W, et al. Compositional optimization of high-solid-loading ceramic cores via 3D printing. Addit. Manuf., 2022, 58: 103054.
[8] Li H, Liu Y S, Colombo P, et al. The influence of sintering procedure and porosity on the properties of 3D printed alumina ceramic cores. Ceram. Int., 2021, 47(19): 27668–27676.
[9] Hu K H, Wang H Y, Lu K, et al. Fabrication of silica-based ceramic cores with internal lattice structures by stereolithography. China Foundry, 2022, 19(5): 369–379.

[10] Dong W J, Li Q L, Chen T C, et al. Effect of sintering temperature on microstructure and properties of 3D printing polysilazane reinforced Al_2O_3 core. China Foundry, 2023, 20(5): 387–394.
[11] Li Q L, Chen T C, Liang J J, et al. Manufacturing of ceramic cores: From hot injection to 3D printing. J. Mater. Sci. Technol., 2023, 134: 95–105.
[12] Zhang Z F, Wang L, Zhang L T, et al. Binder jetting 3D printing process optimization for rapid casting of green parts with high tensile strength. China Foundry, 2021, 18(4): 335–343.
[13] Li X, Su H J, Dong D, et al. Selection strategy of curing depth for vat photopolymerization 3D printing of Al_2O_3 ceramics. Addit. Manuf., 2024, 88: 104240.
[14] Wang P W, Yu R L, Tan R, et al. Preparation of coated sand for selective laser sintering and optimization of baking process of sand moulds. China Foundry, 2023, 20(6): 519–525.
[15] Zhou H R, Yang H, Li H Q, et al. Advancements in machine learning for material design and process optimization in the field of additive manufacturing. China Foundry, 2024, 21(2): 101–115.
[16] Li Q L, An X L, Liang J J, et al. Balancing flexural strength and porosity in DLP-3D printing Al_2O_3 cores for hollow turbine blades. J. Mater. Sci. Technol., 2022, 104(9): 19–32.
[17] Li X, Su H J, Dong D, et al. In-situ $Y_3Al_5O_{12}$ enhances comprehensive properties of alumina-based ceramic cores by vat photopolymerization 3D printing. Addit. Manuf., 2023, 73: 103645.
[18] Li X, Su H J, Dong D, et al. New approach to preparing near zero shrinkage alumina ceramic cores with excellent properties by vat photopolymerization. J. Mater. Sci. Technol., 2024, 193: 61–72.
[19] Niu S X, Wang K, Luo Y S, et al. Enhanced high-temperature dimensional accuracy by fibers in silica ceramic cores prepared through vat photopolymerization 3D printing. Ceram. Int., 2024, 50(14): 25886–25894.
[20] Li Q L, Hou W Q, Liang J J, et al. Controlling the anisotropy behaviour of 3D printed ceramic cores: From intralayer particle distribution to interlayer pore evolution. Addit. Manuf., 2022, 58: 103055.
[21] Mu Y H, Chen J W, An X L, et al. Effect of synergism of solid loading and sintering temperature on microstructural evolution and mechanical properties of 60vol% high solid loading ceramic core obtained through stereolithography 3D printing. J. Eur. Ceram. Soc., 2023, 43(2): 661–675.
[22] Liu W W, Li M S, Nie J B, et al. Synergy of solid loading and printability of ceramic paste for optimized properties of alumina via stereolithography-based 3D printing. J. Mater. Res. Technol., 2020, 9(5): 11476–11483.
[23] He C, Liu X E, Ma C, et al. Digital light processing of Si-based composite ceramics and bulk silica ceramics from a high solid loading polysiloxane/SiO_2 slurry. J. Eur. Ceram. Soc., 2021, 41(14): 7189–7198.
[24] Zhang K Q, Xie C, Wang G, et al. High solid loading, low viscosity photosensitive Al_2O_3 slurry for stereolithography based additive manufacturing. Ceram. Int., 2019, 45(1): 203–208.
[25] Fan J, Li Q L, Jin F N, et al. High solid loading, low viscosity stereolithography 3D printing ceramic cores slurry. Ceram. Int., 2023, 49(24): 40705–40715.
[26] Jin F N, Li Q L, Yang K, et al. Optimisation and application of high solid loading stereolithography 3D printing ceramic cores slurry. Ceram. Int., 2024, 50(2): 3574–3583.
[27] Wang X G, Zhou Y L, Zhou L, et al. Microstructure and properties evolution of silicon-based ceramic cores fabricated by 3D printing with stair-stepping effect control. J. Eur. Ceram. Soc., 2021, 41(8): 4650–4657.
[28] Liu H, Zhang R Z, Wu J M, et al. Effect of $Al(OH)_3$ on the properties of silica-based ceramic cores prepared by laser powder bed fusion combined with vacuum infiltration. Addit. Manuf., 2024, 95: 104527.
[29] Zheng W, Wu J M, Chen S, et al. Improved mechanical properties of SiC fiber reinforced silica-based ceramic cores fabricated by stereolithography. J. Mater. Sci. Technol., 2022, 116: 161–168.
[30] Feng M Z, Wang Z W, Wang W Q, et al. Effect of bimodal particle size distribution on the performance of SiC slurry for maskless vat photopolymerization. J. Eur. Ceram. Soc., 2023, 43(16): 7296–7305.
[31] Gentry S P, Halloran J W. Absorption effects in photopolymerized ceramic suspensions. J. Eur. Ceram. Soc., 2013, 33(10): 1989–1994.
[32] Li T, Zhang Y Z, Duan W Y, et al. A study on the control of the printing accuracy in alumina parts by ceramic stereolithography. J. Eur. Ceram. Soc., 2024, 44(12): 7149–7159.
[33] Fu J C, Yu H J, Wang L, et al. Preparation and properties of UV-curable diamine-based polyurethane acrylate hard coatings. Appl. Surf. Sci., 2020, 533: 147442.
[34] Wu J B, Ma G Z, Li P, et al. Surface modification of nanosilica with acrylsilane-containing tertiary amine structure and their effect on the properties of UV-curable coating. J. Coat. Technol. Res., 2014, 11(3): 387–395.
[35] Xu X H, Zhou S X, Wu J F, et al. Inter-particle interactions of alumina powders in UV-curable suspensions for DLP stereolithography and its effect on rheology, solid loading, and self-leveling behavior. J. Eur. Ceram. Soc., 2021, 41(4): 2763–2774.
[36] Chen Y A, Tan J L, Sun J X, et al. Effect of sintering temperature on the microstructures and mechanical properties of ZrO_2 ceramics fabricated by additive manufacturing. Ceram. Int., 2024, 50(7): 11392–11399.
[37] Park H Y, Yeo J G, Choi J, et al. Ceramic green and fired body with a uniform microstructure prepared using living characteristics of photo-curable cycloaliphatic epoxide: Applicability of cycloaliphatic epoxide in photo-polymerization-based 3D printing. J. Eur. Ceram. Soc., 2022, 42(2): 589–599.
[38] Krieger I M, Dougherty T J. A mechanism for non-newtonian flow in suspensions of rigid spheres. Trans. Soc. Rheol., 1959, 3(1): 137–152.
[39] Bray D J, Gilmour S G, Guild F J, et al. The effects of particle morphology on the analysis of discrete particle dispersion using Delaunay tessellation. Compos., Part A: Appl. Sci. Manuf., 2013, 54: 37–45.
[40] Maniere C, Kerbart G, Harnois C, et al. Modeling sintering anisotropy in ceramic stereolithography of silica. Acta. Mater., 2020, 182: 163–171.